Contents lists available at ScienceDirect

Journal of Molecular Structure

journal homepage: www.elsevier.com/locate/molstruc

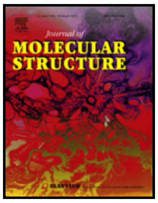

Cu_2O@Zn-Fe LDH core-shell photocatalyst for solar photo-degradation of congo red: An experimental, DFT, and Monte Carlo combined simulation

S. Kiamouche [a, b, *], L. Messaadia [a, *], M. Benamira [c, *], H. Lahmar [d], A. Hamdache [e], S.E. Drif [f], M. Trari [g]

[a] Department of Chemistry, Laboratory of Applied Energy and Materials (LEAM), University of Jijel, Jijel, Algeria
[b] Department of Environmental Engineering, Faculty of Process Engineering, University of Constantine 3 Salah Boubnider, 25000 Constantine, Algeria
[c] Department of Chemistry, Laboratory of Materials Interaction and Environment (LIME), University Mohamed Seddik Benyahia, BP 98, Ouled Aissa, 18000 Jijel, Algeria
[d] Department of Chemistry, LEND Laboratory, University Mohamed Seddik Benyahia, BP 98, Ouled Aissa, 18000 Jijel, Algeria
[e] Department of Process Engineering, Faculty of Sciences and Applied Sciences, Bouira University, Drissi Yahia Street, Bouira 10000, Algeria
[f] Department of Biochemistry and Microbiology, University of M'sila, M'sila, Algeria
[g] LSVAR Laboratory, Faculty of Chemistry (USTHB), 16111 Algiers, Algeria

ARTICLE INFO

Keywords:
Photocatalytic activity
Cu_2O@Zn-Fe LDH
Congo Red dye
Solar radiation
Molecular dynamics
Monte Carlo simulation

ABSTRACT

A significant photocatalytic activity was achieved using Cu_2O surrounded by Zn-Fe layered double hydroxide (LDH) for the degradation of Congo Red (CR) under solar radiation. Photocatalytic tests were conducted with Cu_2O, Zn-Fe LDH, and Cu_2O@Zn-Fe LDH, with experimental conditions optimized for complete CR degradation. The physical and optical properties of Cu_2O, Zn-Fe LDH, and Cu_2O@Zn-Fe LDH were correlated with photoelectrochemical characterization to establish the energy diagram of the Cu_2O@Zn-Fe LDH core-shell/electrolyte system. UV–visible spectroscopy revealed bandgap values of 2.04 eV for Cu_2O and 2.24 eV for Zn-Fe LDH, corresponding to directly allowed transitions. Flat band potentials, determined from capacitance-potential plots, were -0.32 V/SCE for Cu_2O and 0.13 V/SCE for Zn-Fe LDH. Visible light absorption induced electron transfer from the conduction band of Cu_2O (-2.05 V/SCE) to the shallow trapping sites of Zn-Fe LDH (-0.79 V/SCE), enhancing charge carrier separation and accelerating CR degradation. Under solar illumination and optimized conditions (pH ~ 6.78, T ~ 25 °C, catalyst dose of 1 mg/mL), complete degradation of 10 mg/L CR was achieved, with total organic carbon analysis confirming mineralization. The Density Functional Theory (DFT)-optimized structure of CR dye was analyzed to predict reactive sites using Fukui functions, the dual descriptor f_k^2, local, softness $\Delta\sigma_k$, and local philicity $\Delta\omega_k$. The analysis identified the most favorable sites for nucleophilic attack as the N13 (0.0299) and N14 (0.0357) atoms. Based on dynamic and Monte Carlo simulations, the Zn–Fe LDH and Cu_2O@Zn-Fe LDH surfaces exhibited the highest adsorption energy for CR dye, resulting in strong adsorption. This finding is consistent with our experimental studies.

1. Introduction

The chemical structure of Congo Red contains the azo (-N=N-) group, classifying it as an azo dye. It is commonly synthesized from basic azo compounds, with a general molecular formula of $C_{32}H_{22}N_6O_6S_2$. Congo Red is a dark red crystalline powder. This anionic dye is widely used for coloring clothing, paper, and hair, and also functions also as a photosensitizer. Toxicological evaluations have demonstrated that CR is carcinogenic and highly toxic, even at low concentrations [1,2]. As a representative azo dye, CR poses a significant challenge for degradation due to its complex aromatic structure and stability.

Given its environmental and health risks, CR can be removed via photocatalysis, an effective process for treating toxic effluents discharged into rivers, seas and oceans. As an advanced oxidation process (AOPs), photocatalysis is a reliable and efficient strategy for eliminating organic pollutants from water. Effective light ($E_g > h\nu$) excites the semiconductor, generating electron-hole (e^-/h^+) pairs that react with O_2 and H_2O to produce reactive oxygen species (ROS), which degrade resistant pollutants [3–5]. Cu_2O is commonly used in photocatalysis due to its low toxicity and ideal band gap [6,7]. However, the rapid recombination of (e^-/h^+) pairs and the photo-corrosion of Cu_2O limit its photocatalytic performance [7,8].

---

* Corresponding authors.
E-mail addresses: kiamouchesamir@gmail.com (S. Kiamouche), lyamine.messaadia@gmail.com (L. Messaadia), m_benamira@univ-jijel.dz (M. Benamira).

https://doi.org/10.1016/j.molstruc.2025.142701
Received 25 December 2024; Received in revised form 24 April 2025; Accepted 15 May 2025

Several strategies have been explored to enhance the photoactivity of Cu_2O, including doping with noble metal nanoparticles [9], introducing non-metallic elements [10], and coupling Cu_2O with another semiconductor to form a heterojunction [11], as well as coating Cu_2O with layered double hydroxides. These structures, known as core-shell materials, have proven to be particularly promising [12]. They consist of an active material embedded within a protective shell, offering significant advantages over traditional single-material systems [13]. The combination of different materials in a core-shell configuration optimizes charge carrier dynamics, improves light absorption, and enhances overall device performance while mitigating individual weaknesses [14].

According to Wang and al [15], the $Cu_2O@TiO_2$ core-shell material exhibited an efficiency 5.2 times higher than that of pure Cu_2O for naphthalene oxidation. In this study, ZnFe LDHs were proposed to encapsulate Cu_2O due to their promising physicochemical properties. Indeed, the narrow band gap of ZnFe LDH makes it an ideal *n*-type photocatalyst because of its affordable cost, theoretical photocurrent efficiency, and high sensitivity to solar radiation [16]. LDHs are important two-dimensional (2D) materials, classified within the hydrotalcite (HT)-type compound group [16]. These materials consist of positively charged hydroxide layers intercalated with divalent metal ions (such as Ca^{2+}, Zn, Mg^{2+}, and Ni^{2+}) or trivalent metal ions (Al^{3+}, Fe^{3+}, Cr^{3+}, and In^{3+}).

LDHs play a key role not only in photocatalysis [17] but also in a variety of applications related to life sciences [18]. In recent years, LDHs and their composites have been extensively studied in biological, chemical, and environmental processes has been extensively studied [19]. LDHs can be synthesized under mild conditions, particularly via the coprecipitation method. This technique involves adding a base to an aqueous solution containing salts of two different metals, M^{2+} and M^{3+}, which induces the precipitation of metal hydroxides leading to the formation of LDHs [19–21].

Building on recent work on core-shell structures, this study focuses on the use of Cu_2O@Zn-Fe LDH, synthesized via a coprecipitation method, for the CR photodegradation. The impact of pH and the ratios of the combined photocatalysts on photocatalytic performance are explored. Furthermore, to validate the experimental results and analyze the photoactivity of the core-shell structure, a theoretical study is conducted using Density Functional Theory (DFT/SCAN) [22–24]. The goal is to identify the optimal structure in the aqueous phase, predict the reactivity of the CR molecule, and examine the influence of operational parameters such as Fukui indices, the local dual descriptor f_k^2, local softness $\Delta\sigma_k$, local philicity $\Delta\omega_k$, and the electrostatic potential (ESP) surface map are used to analyze the reactive sites of the CR molecule. Based on both experimental and theoretical findings, different pathways for photoactivity and degradation are also discussed.

2. Materials and methods

2.1. Synthesis

The synthesis of Cu_2O nanoparticles was carried out by mixing $Cu(NO_3)_2·3H_2O$ (Sigma-Aldrich, 98 %) (0.1 M) and glucose (Sigma-Aldrich, > 99.5 %) (0.5 M) in 100 mL of distilled water. The solution is stirred at 80 °C until its color changes from blue to bluish-green. Subsequently, a NaOH (Sigma-Aldrich, > 99 %) solution (1 M) was added dropwise until reaching pH 11.5, while maintaining stirring at 80 °C for 90 min. During this step, the solution's color gradually transitions to brick red. Finally, the obtained product was dried at 100 °C for 4.5 h [25].

The Zn–Fe layered double hydroxide was prepared following the protocol described below: aqueous solutions (50 mL) containing $ZnCl_2·6H_2O$ (Sigma-Aldrich, ≥ 98 %) and $FeCl_3·6H_2O$ (Biochem, ≥ 98 %) were gradually added dropwise to 50 mL of distilled water under stirring at room temperature. During the coprecipitation process, the pH of the reaction mixture was maintained constant at 9 by simultaneous addition of NaOH solution (2 mol·L^{-1}). The resulting suspension was then diluted in 200 mL with distilled water (DI) and stirred for 12 h. During the oxidation step, the pH was adjusted to approximately 8 using a NaOH solution. The resulting solids were separated via vigorous centrifugation, rinsed twice with deionized (DI) water, and subsequently dried under vacuum for 48 h using a lyophilizer [26,27].

For the synthesis of Cu_2O@Zn–Fe LDH, 200 mg of Cu_2O Nano-cubes were dispersed in 100 mL of DI in a Pyrex beaker. Subsequently, 0.8 mmol of $ZnCl_2·6H_2O$ and 0.4 mmol of $FeCl_3·6H_2O$ were added to the suspension under continuous stirring. Next, 20 mL of a sodium thiosulfate solution (Sigma-Aldrich, ≥ 99,5 %) (1 M, $Na_2S_2O_3$) were added to the mixture, and the beaker was placed in a thermostated water bath maintained at 65 °C for 2 h. Finally, the precipitates were collected by centrifugation, thoroughly washed with DI and ethanol, and dried in an oven at 80 °C [28].

2.2. Instrumentation

To characterize the crystalline structure of Cu_2O, Zn-Fe LDH, and Cu_2O@Zn–Fe LDH samples, a Bruker X-ray diffractometer (XRD) "D8 Advance", equipped with a copper anticathode, an X-ray tube, a primary Ge (111) monochromator focusing (Cu Kα), and a "Vantec" 1-D position-sensitive detector was used. The analyses were conducted over a 2θ range (10 - 80°), with steps of 0.016° and a counting time of 5 s per step. The XRD data analysis was conducted using HighScore Plus software, with the 2023 database version. The surface morphology and elemental composition of the Cu_2O, Zn-Fe LDH and Cu_2O@Zn-Fe LDH semiconductors were examined by scanning electron microscopy (SEM) and energy dispersive X-ray spectroscopy (EDS) using a Thermo Scientific Quattro S microscope.

The FT-IR analysis was performed with a Jasco FT/IR-4600 spectrometer, covering a wavelength range from 7800 to 350 cm^{-1}, with a maximum resolution of 0.7 cm^{-1}. Textural properties, including surface area, pore volume, and pore diameter, were determined by the BET method based on N_2 adsorption-desorption isotherms measured with an Autosorb iQ3 (Quantachrome Instruments) system. Samples weighing between 200 and 300 mg were degassed under vacuum at 200 °C for 8 h. High N_2 gas was used as the adsorbate. For optical characterization, a UV–Vis Specord 210 Plus spectrophotometer was used to measure the diffuse reflectance data in the range of 200 to 800 nm, using PTFE as the reference.

The electrochemical characterization was carried out at room temperature, using a saturated calomel electrode (SCE) as the reference electrode and a platinum electrode as the auxiliary electrode. Mott-Schottky (MS) analysis was performed in a Na_2SO_4 (0.5 M) electrolyte at a frequency of 10 kHz, with a potential sweep rate of 5 mV·s^{-1}. The point of zero charge (pH_{pzc}) was determined by the drift method by measuring the initial and final pH values of 50 mL of $NaNO_3$ (0.1 M) solution containing 0.05 g of Cu_2O, Zn-Fe LDH, and Cu_2O@Zn-Fe LDH at different pHs, adjusted using HCl and NaOH solutions. The mixtures were allowed to equilibrate at 25 °C in a thermostatic shaker for 18 h. The pHpzc was determined from the intersection of the lines "initial pH and final pH". Total organic carbon (TOC) analysis of the CR-laden water was carried out using a TOC analyzer with a non-dispersive infrared (NDIR) source (Shimadzu, model TOC-L).

Photodegradation of CR was performed in a double-jacketed Pyrex reactor connected to a thermostated bath. 100 mg of powder was magnetically dispersed in 100 mL of CR solution (10 mg/L). After an adsorption period (2 h), the reactor was exposed to solar radiation (~ 100 mW/cm^2) and the temperature was set to 25 °C. Aliquots of 3 mL were periodically withdrawn and the CR concentration was titrated with a UV-visible spectrophotometer (Simadzu UV1800), by measuring the absorbance of a CR solution at λ_{max} in accordance with the Beer-Lambert law. The concentration at time (***t***) C_t is deduced by linear interpolation of the constructed graph; the percentage of degradation is calculated based on the following relationship (Eq. (1)):

$$(\%) = \frac{C_{eq} - C_t}{C_{eq}} \times 100 \qquad (1)$$

C_{eq} and C_t are the equilibrium concentrations after adsorption in the dark and at time t, respectively.

2.3. Computational chemistry studies

The Dmol^3 module, integrated within the BIOVIA Material Studio software [29], played a pivotal role in our density functional theory (DFT) calculations. Specifically, we conducted custom geometry optimization for the structure of CR in the aqueous phase. To achieve this, we employed the SCAN functional, which is a meta-generalized gradient approximation (meta-GGA). Our objective was to predict the reactivity of the CR molecule, considering that the CR pollutant can undergo degradation under oxidation or reduction conditions.

For the atomic orbital basis set, we utilized the Double Numerical Plus Polarization (DNP) 4.4 in our calculations. Additionally, we set the global orbital cutoff to 4.5 Å to define more precise parameters governing the atomic orbital cutoffs. To simulate a solvent environment, we employed the Conductor-like Screening Model (COSMO) with a dielectric constant of 78.540 for water, adhering to the 'fine quality' convergence criteria.

In the DFT calculation, we adhered to the following convergence criteria:

- Maximum displacement between cycles: Less than 0.005 Å.
- Maximum self-consistent field (SCF) tolerance: 10^{-5} Hartree (Ha).
- Maximum force per atom: 0.002 Ha/Å.

The Fukui indices (FI) played a crucial role in our study. These indices have widespread application in predicting the reactive sites for electrophilic, nucleophilic, and radical attacks. We analysed the FI using the following formulas (Eqs. (2–4)) [30,31]:

- The highest value of (f_k^+) is given by:

$$q_k\,(N+1) - q_k\,(N) \approx \rho(r)^{LUMO} \qquad (2)$$

which suggests a nucleophilic attack.

- The highest value of (f_k^-) is given by:

$$q_k\,(N) - q_k\,(N-1) \approx \rho(r)^{HOMO} \qquad (3)$$

indicating an electrophilic attack.

- Similarly, the highest value of (f_k^0) is calculated as:

$$\left[q_k\,(N+1) - q_k\,(N-1)\right]/2 \qquad (4)$$

which corresponds to a radical attack. Here, ($q_k\,(N)$, $q_k\,(N+1)$and $q_k\,(N-1)$ represent the charges of atom (k) in the neutral, anionic, and cationic molecules, respectively.

The dual descriptor f_k^2, also known as the second-order Fukui function, is a reactivity descriptor used in computational chemistry to identify the reactivity sites within a molecule. The dual descriptor provides insight into the regions of a molecule that are more likely to undergo nucleophilic or electrophilic attacks [32,33].

If ($f_k^2\,(r) > 0$ at a point r, it indicates that the site is more likely to attract nucleophiles (Nucleophiles are electron-rich species that donate electrons). If $f_k^2\,(r) < 0$ at a point r, it indicates that the site is more likely to attract electrophiles. Electrophiles are electron-deficient species that accept electrons.

In addition, local softness $\Delta\sigma_k$ and local philicity $\Delta\omega_k$ used to describe the reactivity of atoms in molecule, can be defined as: $\sigma_k^\alpha = Sf_k^\alpha$and $\omega_k^\alpha = \omega f_k^\alpha$.

S and ω are the global softness and the global philicity respectively, and $f_k^\alpha$is the Fukui function for site k with respect to a specific type of attack (α). Local softness measures the propensity of a site to react with a nucleophile (α = +), electrophile (α = −), or radical (α = 0).

The Electrostatic Potential Surface (EPS) serves as a valuable tool for identifying reactive chemical sites within compounds. By visualizing the electron density iso-surface using distinct colors, we gain insights into the electrostatic potential distribution;

- Blue Region: This area corresponds to the most positive electrostatic potential. It exhibits a scarcity of electrons and carries a positive charge. Such regions are conducive to nucleophilic attacks.
- Yellow Region: Heteroatoms, such as chlorine (NH_2, SO_3), manifest the most negative electrostatic potential. These regions favor electrophilic attacks.
- Green Region: The zero potential zone lacks any significant charge.

2.4. Molecular dynamics and Monte Carlo (MC) simulation

Molecular Dynamics (MD) simulations indeed serve as powerful tools for comprehending the affinity of compounds and the intricate degradation mechanisms of pollutants [34]. Through these simulations, we gain valuable insights into the behavior, interactions, and transformations of molecules. The Cu_2O@Zn-Fe LDH model was constructed by depositing two layers of Zn-Fe LDH of the (003) facet onto the Cu_2O crystal. The system was immersed in an aqueous solution containing 200 water molecules. A vacuum slab with a thickness of 35 Å was generated above the LDH surfaces. To mitigate arbitrary boundary effects, we cleaved the semiconductor surface to a thickness of 3 Å. The selection of the Zn-Fe LDH (003) and Cu_2O (111) surfaces was guided by X-ray diffraction (as shown in Fig. 1). We employed a supercell surface with dimensions of 4 × 4 for Zn-Fe LDH and 12 × 12 for Cu_2O to simulate strong interactions. The simulation was conducted using boxes with dimensions of (a = 37.844 Å, b = 37.844 Å and c = 44.437 Å) for Zn-Fe LDH (003) and of (a = 50.459 Å, b = 25.229 Å and c = 26.437 Å) for Cu_2O (111).

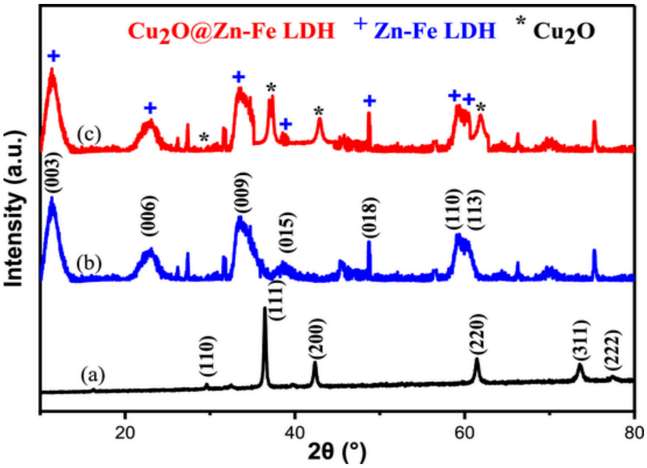

Fig. 1. The XRD patterns of the as prepared a) Cu_2O, b) Zn-Fe LDH and c) Cu_2O@Zn-Fe LDH.

The Monte Carlo (MC) simulation was conducted using the Adsorption Locator module, which is part of the BIOVIA Materials Studio package [29], to elucidate the adsorption mechanism of CR on the surfaces of Cu_2O@ZnFe-LDH, Zn-Fe LDH and Cu_2O respectively in 200 H_2O. For geometry optimization, we employed the COMPASS III force field [35]. The simulation was performed using the adsorption Forcite calculation module, employing a time step of 1 fs and a total simulation time of 500 ps under the NVT ensemble (where N represents the number of particles, and the ensemble considers temperature and volume) at 25 °C [36].

3. Results and discussion

3.1. Structural, morphological, and optical properties

The crystalline structure of the as-prepared Cu_2O was characterized using XRD analysis. According to the JCPDS card no 78–2076 [7], all the peaks observed in the pattern (Fig. 1) correspond to the cuprite phase (space group: Pn-3 m), crystallizing in a cubic symmetry. Furthermore, Fig. 1 shows that all peaks of Zn-Fe LDH are well indexed with rhombohedral symmetry (space group: R-3 m), in agreement with the JCPDS Card N° 38–0486 [18]. For the core-shell Cu_2O@Zn-Fe LDH material, the XRD peaks associated with both Cu_2O and Zn-Fe LDH remain almost unchanged, as shown in Fig. 1.

The surface and morphology of the prepared Cu_2O, Zn-Fe LDH, and Cu_2O@Zn-Fe LDH powders are visualized by SEM analysis. The SEM image of Cu_2O (Fig. 2**a**) reveals the formation of a large number of Nano-cubes while the morphology of the synthesized Zn-Fe LDH (Fig. 2**b**) exhibits a lamellar structure with an average thickness of 100 nm, clearly visible in the SEM images. The particles display a less uniform morphology, characterized by the coexistence of nanocubes of various sizes. For the core-shell Cu_2O@Zn-Fe LDH particles, significant aggregation is observed, with the disappearance of sharp edges, as shown in Figs. 2c and 2d The Cu_2O nanoparticles are distinctly different from the Zn-Fe LDH nanoparticles.

The FTIR spectra of Cu_2O@Zn-Fe LDH were recorded in the wavelength range (600 - 4000 cm^{-1}) to identify the functional groups present (Fig. 3). Absorption peaks below 1000 cm^{-1} correspond to the inorganic vibrations of O-M-O and M-O groups ($M = Cu^{2+}$, Zn^{2+}, and Fe^{2+}) [37]. A distinct peak at 1372 cm^{-1} is associated with the carbonate anion (CO_3^{2-}) located in the interlayer region of the LDH [37]; their presence is probably linked to the dissolution of atmospheric CO_2 in the distilled water used during synthesis [26]. Furthermore, the peak at 1600 cm^{-1} is attributed to the bending vibrations of water molecules present in the interlayer region [7]; the broad band (3350 cm^{-1}) is due to hydroxyl (O—H) groups on the surface of the LDH layers and embedded in water molecules [18].

The BET analysis forms the basis for various low-temperature gas adsorption methods. The specific surface areas of Cu_2O, Zn-Fe LDH, and Cu_2O@Zn-Fe LDH were calculated using the analytical treatment of the experimental data of N_2 adsorption isotherm, as shown in Eq. (5):

$$\frac{P}{V\left(P_0-P\right)}=\frac{1}{V_m\times C}+\frac{P}{P_0}\times\frac{C-1}{V_m\times C} \tag{5}$$

P is the equilibrium pressure, P_0 the saturated vapor pressure of the adsorbate, V the volume of adsorbed gas per gram of solid at pressure P, V_m the volume of gas required to form a complete monolayer of adsorbate, and C is a constant characteristic of the gas-solid system.

The monolayer adsorption volume V_m is calculated using the BET equation (Eq. (5)), and the specific surface area of Cu_2O, Zn-Fe LDH, and Cu_2O@Zn-Fe LDH is determined using Eq. (6):

$$S_{BET}=\left(\sigma\times V_m\times N_a\right)/V_M \tag{6}$$

σ represents the area occupied by a single N_2 molecule ($\sigma = 16.2$ Å^2), N_a the Avogadro's number, and V_M the molar volume. The BET results for Cu_2O, Zn-Fe LDH, and Cu_2O@Zn-Fe LDH are shown in Fig. 4. According to the BET analysis, the specific surface area (S_{BET}) of Zn-Fe LDH particles is higher (44.12 $m^2\ g^{-1}$) compared to Cu_2O (30.12 $m^2\ g^{-1}$) and Cu_2O@Zn-Fe LDH (38.87 $m^2\ g^{-1}$).

The optical band gap (E_g) allows to quantify the fraction of solar flux converted into photocatalytic form. It can be calculated using the Munk-Kubelka equation (Eq. (7)) [38,39]:

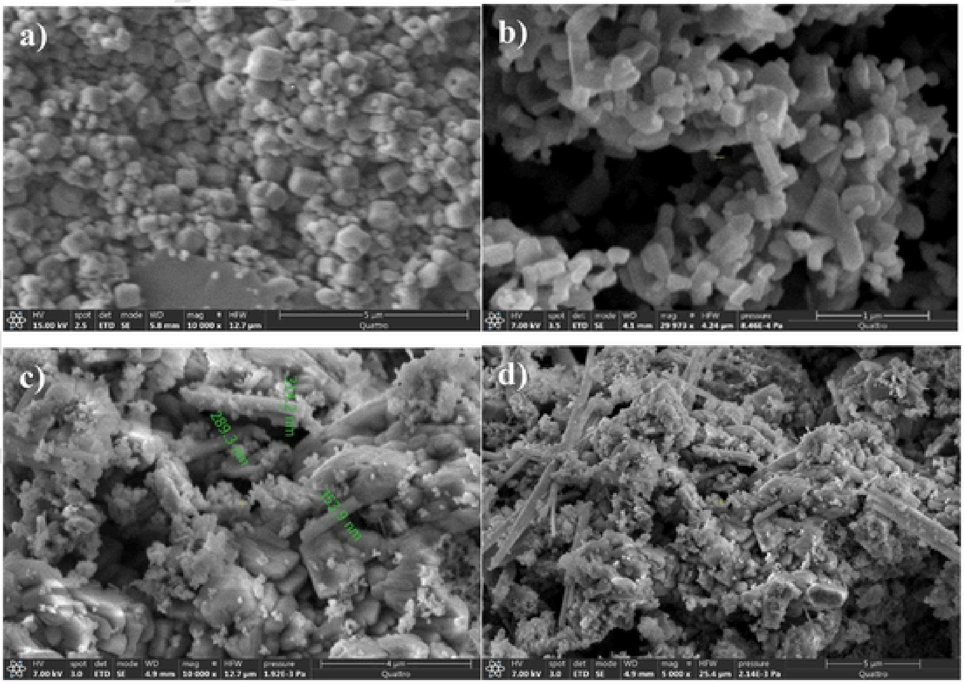

Fig. 2. SEM images of the: a) Cu_2O, b) Zn-Fe LDH, c and d) Cu_2O@Zn-Fe LDH.

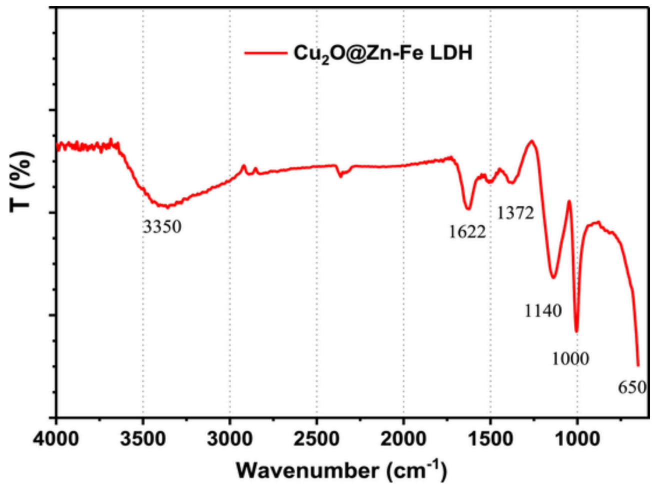

Fig. 3. FTIR spectrum of Cu_2O, Zn-Fe LDH and Cu_2O@Zn-Fe LDH.

$$F\left(R_{\infty}\right) = \left(1 - R_{\infty}\right)^{2} / 2R_{\infty} \tag{7}$$

The converted UV-visible absorption spectrum is used to obtain the diffuse reflectance of Cu_2O, Zn-Fe LDH, and Cu_2O@Zn-Fe LDH (Fig. 5**a** and 5**c**). The optical band gap (E_g) is determined by extrapolating the linear portion of $(F(R)\ h\upsilon)^2$ to $h\nu$-axis. For Cu_2O, a direct optical transition is observed, at 2.04 eV (Fig. 5**b**). In the case of Zn-Fe LDH, a direct allowed transition is observed, with a gap of 2.24 eV (Fig. 5**d**). The E_g values for Cu_2O and Zn-Fe LDH are in good agreement with previous studies [7,27] and confirm the ability of Cu_2O and Zn-Fe LDH to absorb in the visible region.

In general, when the solution's pH exceeds the pHpzc, the photocatalyst particles acquire a negative charge, favorable for adsorbing cationic pollutants. Conversely, below pHpzc, the particles have rather a tendency to adsorb negatively charged pollutants. The of the solution thus plays a critical role in the selective degradation of pollutants. The isoelectric point values (pH_{pzc}) of Cu_2O, Zn-Fe LDH, and Cu_2O@Zn-Fe LDH reflect the surface charge behavior of these compounds in response to changes in the solution's pH. The pH_{pzc} is a key parameter for predicting the surface charge of the photocatalyst under the working conditions. The pH_{pzc} values were determined using the pH drift method. The solution's pH was adjusted using HCl or NaOH. Fig. 6 illustrates the relationship between the initial pH and the difference between the initial and final pH.

Cu_2O exhibits an isoelectric point of 9.28, consistent with values reported in the literature [7]. The pH_{pzc} value indicates that the surface of Cu_2O is positively charged at pH levels below 9.28 and negatively charged at pH levels above 9.28 [40]. The LDHs show isoelectric points similar to those reported in the literature, with val[ues of 7.72 for Zn-Fe LDH and 8.82 for Cu_2O@Zn-Fe LDH [41].

3.2. Electrochemical characterization

The flat band potential (V_{fb}) is a crucial physical parameter for determining the band structure of synthetic semiconductors, predicting their photocatalytic activity, and forecasting interfacial reactions. The

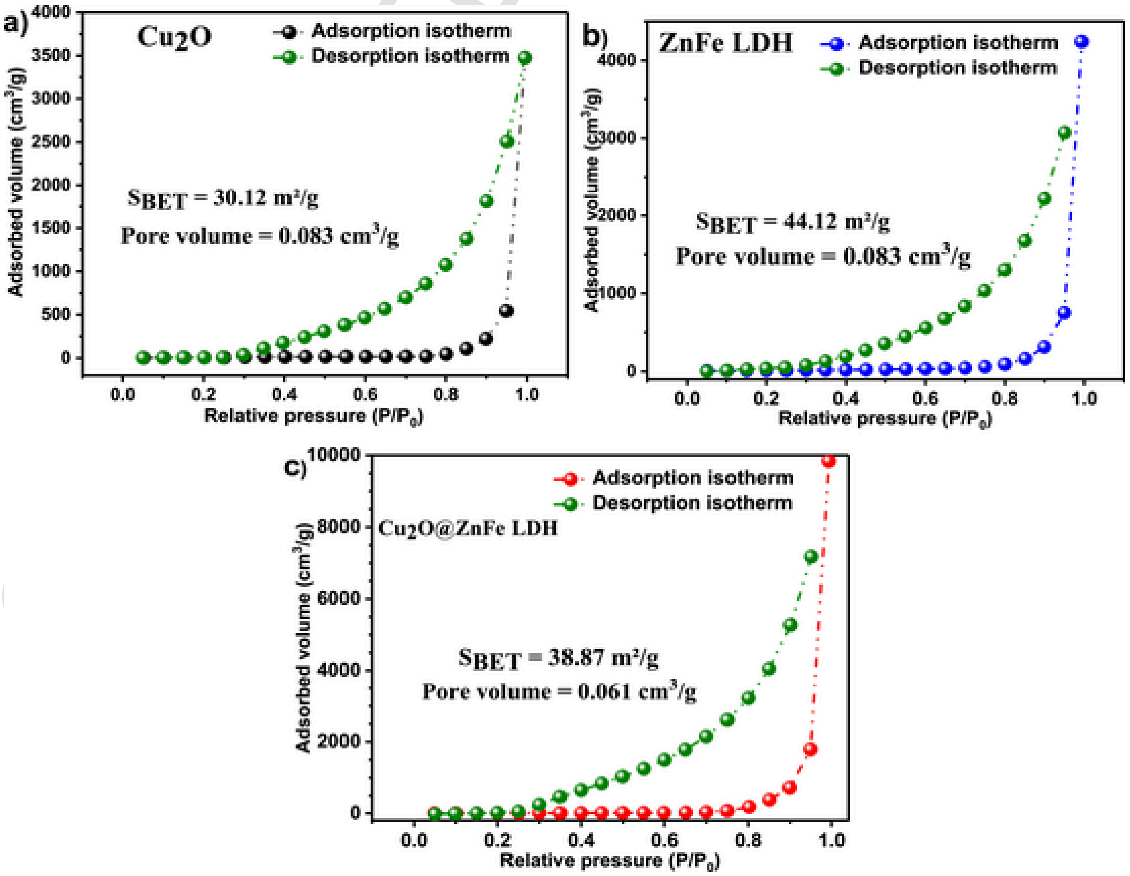

Fig. 4. Nitrogen adsorption-desorption isotherm of: a) Cu_2O, b) Zn-Fe LDH and c) Cu_2O@Zn-Fe LDH.

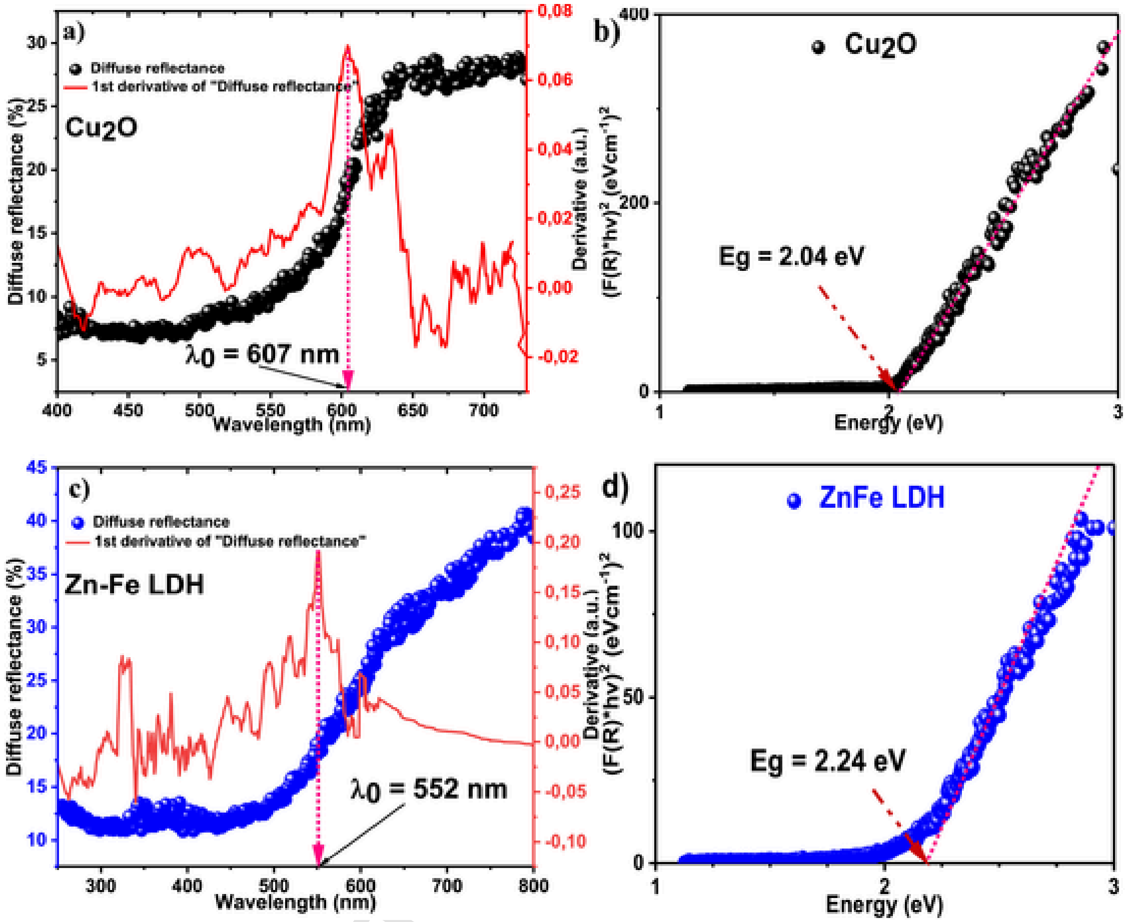

Fig. 5. a), c) Diffuse reflectance UV–vis spectrum of Cu_2O and Zn-Fe LDH, b), d) direct optical transition of Cu_2O and Zn-Fe LDH.

Mott-Schottky plot of the interface capacitance can be used to determine this parameter by applying the following Eq. (8):

$$\frac{1}{C^2} = \left(2/e\varepsilon_r\varepsilon_0 N_d A^2\right)\left[\left(V - V_{fb}\right) - KT/e\right] \quad (8)$$

C is the capacitance of the space charge layer, ε_r is the relative dielectric constant of Zn-Fe LDH and Cu_2O at 25 °C, ε_0 is the dielectric constant of vacuum, N_d is the free carrier density (site/m^3), K is the Boltzmann constant, T is the absolute temperature, and V is the applied electric potential.

The positive slope of the Zn-Fe LDH curve indicates n-type behavior, whereas the negative slope of Cu_2O is characteristic of p-type behavior. The x-intercepts of the linear plots at $C^{-2} = 0$ give the flat band potentials V_{fb}, +0.13 V for Zn-Fe LDH and −0.31 V for Cu_2O. Table 1 presents the results of several physicochemical properties of Cu_2O and Zn-Fe LDH.

Fig. 7

3.3. Photocatalysis

Photocatalysis is one of the advanced oxidation processes that has garnered increasing attention in recent years. This process involves the generation of highly reactive radical intermediates, such as hydroxyl radicals ($^\bullet OH$) and superoxide radicals ($O_2^{\bullet -}$) [44]. These free radicals react much faster than most conventional oxidants, including ozone (O_3) and hydrogen peroxide (H_2O_2). Based on the optical and electrochemical properties of Cu_2O and Zn-Fe LDH, the energy diagram of the Cu_2O@Zn-Fe LDH heterogeneous system can be predicted. The positions of the VB and CB relative to the vacuum level can be determined using Eqs. (9) and (10) (Fig. 8) [45].

$$E_{VB} = 4.74 + e\ V_{fb} + 0.059\ \left(pH - pH_{pzc}\right) + E_a \ \text{(Type p)} \quad (9)$$

$$E_g = E_{VB} - E_{CB} \quad (10)$$

When Cu_2O is exposed to sunlight, electrons (e^-) are excited from VB (= −0.01 V) to CB (= −2.05 V), thereby creating holes (h^+) in VB. This process leads to the formation of (e^-/h^+) pairs, as described by Eq. (11):

$$Cu_2O + h\nu \rightarrow h^+\ (VB) + e^- - (CB) \quad (11)$$

The photo-electrons are transferred from CB of Cu_2O to that of Zn-Fe LDH (−0.05 V). Similarly, the holes can migrate from Zn-Fe LDH-VB (2.19 V) to Cu_2O-VB (−0.01 V). Preventing the recombination of (e^-/h^+) pairs through efficient separation of photogenerated carriers and the formation of a core-shell heterostructure is a well-recognized strategy to improve photoactivity and has been widely employed over the past decades [46]. In this case, the generation of $O_2^{\bullet -}$ and $^\bullet OH$ radicals are not expected, as the conduction band Zn-Fe LDH-CB is less negative than the redox potential of ($O_2/O_2^\bullet$) (−0.33 V vs. NHE), and the valence band Cu_2O-VB does not match the redox potential of ($H_2O/^\bullet OH$) (1.99 V vs. NHE) [47]. Hence, it cannot reduce O_2 into $O_2^\bullet$ and h^+ cannot oxidize OH^- or H_2O to produce radical $^\bullet OH$.

However, based on the energy diagram of the Cu_2O@Zn-Fe LDH heterosystem, a Z-scheme mechanism has been proposed. The positions of VB and CB of Cu_2O are higher than those of Zn-Fe LDH. The high oxidation potential holes in Zn-Fe LDH-VB can react with H_2O to generate

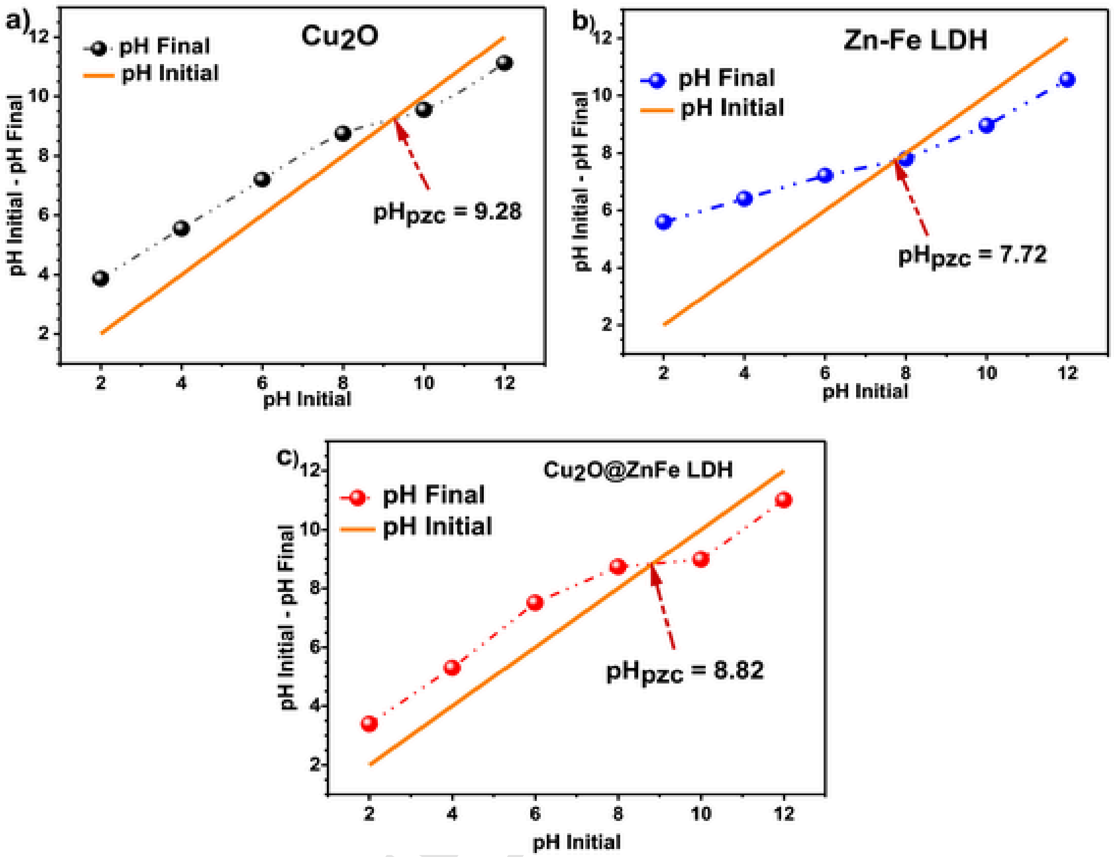

Fig. 6. Point of zero charge (pH_{pzc}) of: a) Cu_2O, b) Zn-Fe LDH and c) Cu_2O@Zn-Fe LDH determined by the pH drift method.

Table 1
Crystallographic information physicochemical properties of Cu_2O and Zn-Fe LDH.

Parameters	Cu_2O	Zn-Fe LDH
Space group	Cubic Pn-3 m	Rhombohedral R-3m
$S_{BET}(m^2/g)$	30.12	44.12
E_g (eV)	2.04	2.24
E_a (eV)	0.48 [42]	0.12 [43]
V_{fp} (V_{SCE})	−0.31 V	0.13 V
E_{VB} (V_{SCE})	−0.01 V	2.19 V
E_{CB} (V_{SCE})	−2.05 V	−0.05 V
pH_{pzc}	9.28	7.72

$^{\bullet}OH$ radicals and/or directly oxidize CR molecules. Additionally, Cu_2O-CB is lower than the redox potential of ($O_2/O_2^{\bullet -}$), enabling the reduction of O_2 to $O_2^{\bullet -}$. The electrons in Zn-Fe LDH-CB migrate to recombine with the holes in Cu_2O-VB. Meanwhile, the accumulated electrons in Cu_2O-CB reduce O_2 to $O_2^{\bullet -}$ while the holes in the Zn-Fe LDH-VB react with H_2O to produce $^{\bullet}OH$ radicals.

The conditions for evaluating the photodegradation of CR are the following: CR concentration = 10 mg/L, pH 6.78, 25 °C and catalyst dose = 1 mg/mL. The experiments were conducted on a sunny day in June. Magnetic stirring was applied in a reactor containing 100 mL of CR solution, and tests were carried out with Cu_2O@Zn-Fe LDH. The pure Cu_2O and Zn-Fe LDH results were also included for comparison.

The best results are achieved with Cu_2O@Zn-Fe LDH, with a high degradation rate of CR within 120 min. under sunlight, outperforming both Cu_2O and Zn-Fe LDH. The formation of a core-shell Cu_2O@Zn-Fe LDH structure accounts for the significant enhancement in photocatalytic activity by reducing the recombination of (e^-/h^+) pairs through a cascade band structure (Fig. 9**a**). The smaller gap of Cu_2O contributes to improve photoactivity. However, a substantial enhancement in CR degradation is achieved through the Z-scheme mechanism facilitated by the core-shell Cu_2O@Zn-Fe LDH structure.

To study the pH effect on the photodegradation, experiments were conducted at four pHs (3, 6.78, 10, and 12) over 120 min. using 100 mL of CR at 10 mg/L and 100 mg of photocatalyst (Fig. 10**a**). On the basis of pHpzc results, lower adsorption is expected at pH > pHpzc due to the negative charges on the surface of the anionic dye (CR) and the photocatalyst. The photocatalytic efficiency under solar irradiation showed no significant change over a broad pH range. It has been observed that the anionic dye CR is more sensitive to the pH of the solution than the cationic dye.

The degradation rate of CR for all the photocatalysts tested was maximized at pH 3, which aligns with the pHpzc results. Indeed, the surface charge of the powder becomes positive (protonated) when electrostatic attraction dominates, leading to strong adsorption and thus enhanced removal of CR.

TOC analyses (Fig. 10**b**) were performed to quantify the mineralization of the organic matter present in the CR solution [48]. Its efficiency was evaluated at different irradiation time intervals, both in the presence and absence of the Cu_2O@Zn-Fe LDH photocatalyst. The results, presented in Fig. 10**b**, show an initial decrease in TOC corresponding to the amount of CR dye remaining in solution and adsorbed onto the surface of Cu_2O@Zn-Fe LDH after reaching equilibrium under dark conditions (120 min). The TOC removal efficiency increased with longer exposure to sunlight. After 60 min. of irradiation, TOC was reduced by 60 %. At 120 min., the experimental data demonstrated that the majority of CR was completely mineralized through the photocatalytic oxidation.

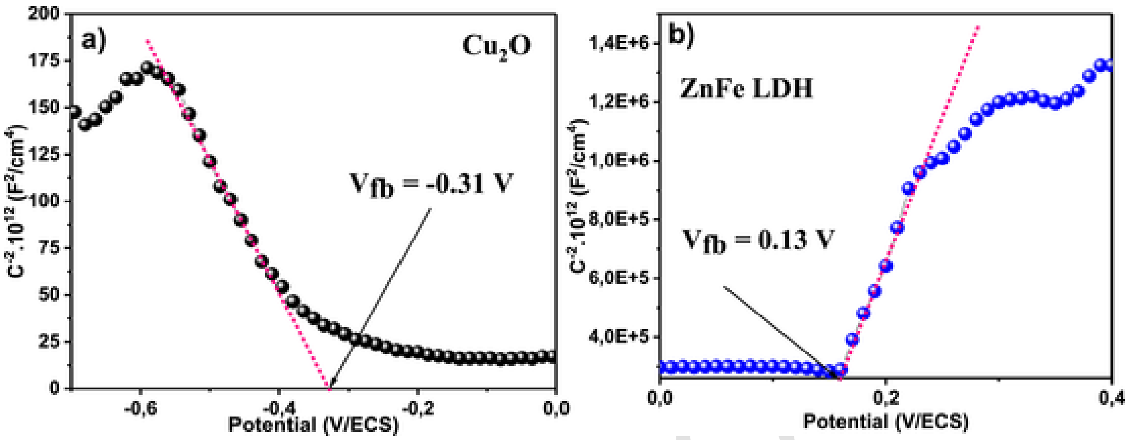

Fig. 7. The Mott Schottky plots of a) Cu$_2$O, b) Zn-Fe LDH; test system: pH ~ 8, electrolyte: 0.5 M Na$_2$SO$_4$, frequency 10 kHz.

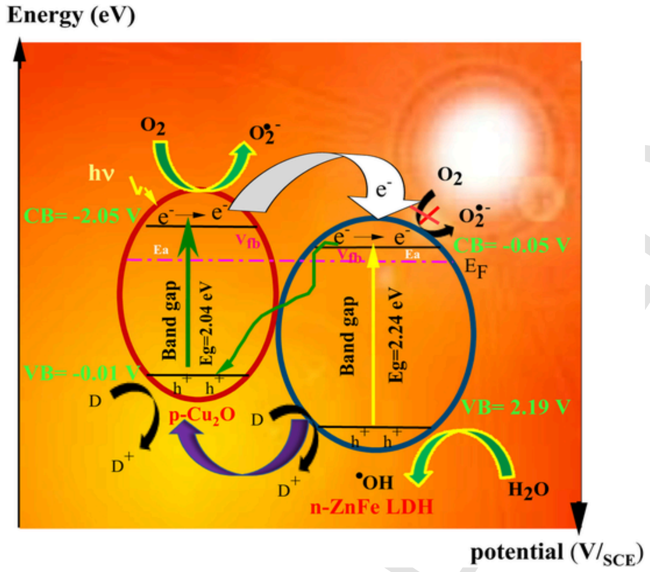

Fig. 8. The energy band diagram of Cu$_2$O@Zn-Fe LDH /CR electrolyte with Z-scheme mechanism.

3.4. Reactivity of Congo red dye

The optimized structure, determined using DFT/SCAN in the aqueous phase (Fig. 11**a**), was employed to predict the reactivity site of CR dye and elucidate the Fukui functions (f^+, f^-,f^0) [49,50]. The results are presented in Fig. 11**b** and **Table S1**. The Fukui indices (FIs) indicate a radical attack on active sites of the CR molecule, which are prone to gaining electrons, thus suggesting a nucleophilic attack. As can be deduced from Fig. 11**b** and **Table S1**, the higher positive part of the f^+function is localized at N 14 (0.062), N13 (0.054), N16 (0.048), N15 (0.029). These atoms represent the greatest reactive sites and are utmost susceptible to nucleophilic attack. However, the most negative part of the f^-function is localized at N12 (0.058), N11 (0.033), N16 (0.032), C26 (0.045), and C22 (0.032) representing the most favorable sites for an electrophilic attack. Similarly, the highest f^0 values are observed at atoms N12 (0.042), N16 (0.040), N14(0.037), N13 (0.033) and N11(0.031), indicating that these sites are the most susceptible to free radical attacks.

In addition, the estimated values of dual descriptors, presented in Table S of the supplementary information, enable us to promptly identify the preferable sites for nucleophilic attacks (f_k^2, $\Delta\sigma_k$, and $\Delta\omega_k > 0$) as well as the preferable sites for electrophilic attacks (f_k^2, $\Delta\sigma_k$, and $\Delta\omega_k < 0$) within the system at point r refer to Fig. 12.

Fig. 12 identifies the most reactive sites on the Congo Red (CR) dye, which can interact with the semiconductor surface. It can be seen that the local philicity ($\Delta\omega_k$) of the CR dye is primarily localized at the most reactive sites, which include specific nitrogen atoms: N13 (0.520659), N14 (0.622251), N16 (0.203184), and N15 (0.190485), as well as some carbon atoms: C23 (0.177786), C45 (0.114291), C28 (0.101592), and C33 (0.101592). This indicates the sites for nucleophilic attacks and how likely an atom of the CR dye is to either donate or accept electrons during interaction with the semiconductor.

On the other hand, the local dual descriptor $f_k^2 > 0$ values are found in the N13 (0.041) and N14 (0.049) atoms, indicating that these sites are favorable for nucleophilic attacks. Additionally, the local softness ($\Delta\sigma_k > 0$) values, which also identify the preferable sites for nucleophilic attacks, are found in the N13 (0.0299) and N14 (0.0357) atoms.

Fig. 13**a** presents the three-dimensional plots of the ESP utilized as an effective method for identifying the chemical reactivity sites in compounds. The blue color indicates regions of positive electrostatic potential, where electron density is lower. These regions are often associated with nucleophilic active region. The yellow regions indicate areas of the most negative electrostatic potential in heteroatoms, such as (SO$_3$), which favor electrophilic attacks, while the green regions illustrate areas of zero potential. Our results clearly indicate that the higher positive electrostatic potential is distributed over the entire molecule except for the root SO$_3$. These regions are favorable sites for nucleophilic attacks.

Similarly, the negative regions of electrostatic potential are localized over the SO$_3$ group of the CR dye, making them favorable sites for electrophilic attacks.

Additionally, another crucial parameter for understanding the electronic structure and reactivity of the system is electron density (Fig. 13**b**), which refers to the distribution of electrons within a molecule. The total electron density map aids in comprehending the chemical behavior of the dye. Regions with low electron density (blue areas) may interact with semiconductors such as Cu$_2$O, Cu$_2$O@Zn-Fe LDH and Zn-Fe LDH in the environment, leading to degradation [7].

3.5. Adsorption studies of Congo red

Molecular dynamics (MD) and Monte Carlo (MC) simulations, utilizing the adsorption locator module, were employed to determine the lowest-energy adsorption configurations between the CR dye and the semiconductors Cu$_2$O, Cu$_2$O@Zn-Fe LDH, and Zn-Fe LDH on their sur-

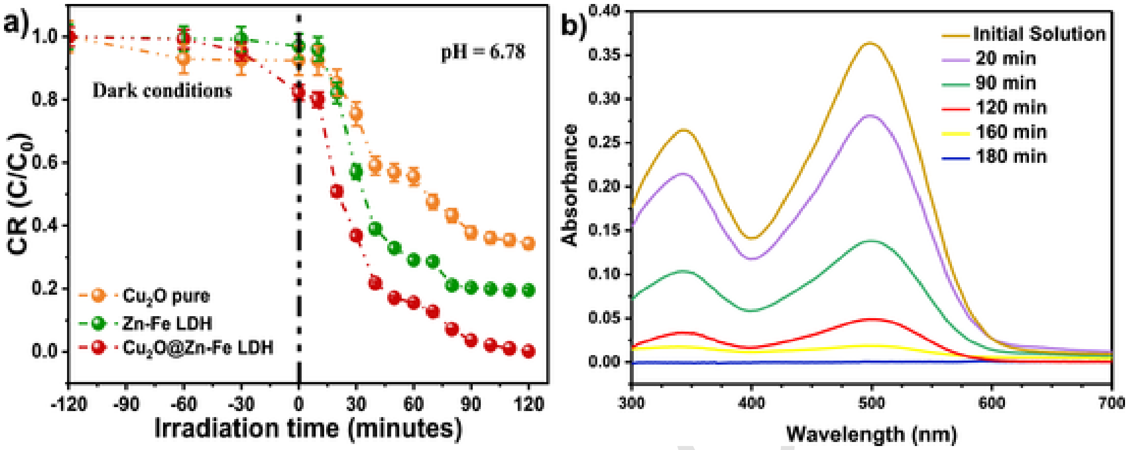

Fig. 9. a) a Kinetics of the CR photodegradation (pH ~ 6.78, T ~ 25 °C, [CR] = 10 mg/L, catalyst dose: 1 mg/1 ml), b) UV–Vis photodegradation spectrum of CR (10 mg/L) over Cu$_2$O@Zn-Fe LDH photocatalyst.

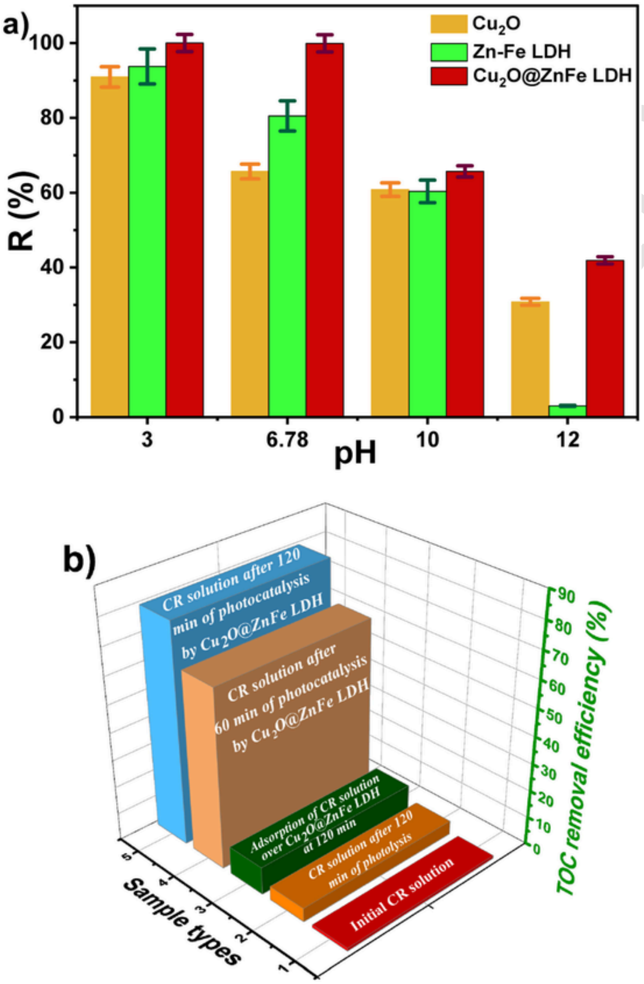

Fig. 10. a) Effect of pH on the photodegradation of CR (10 mg/L) over Cu$_2$O, Zn-Fe LDH, and Cu$_2$O@Zn-Fe LDH photocatalysts. b) Removal efficiencies of TOC by Cu$_2$O@Zn-Fe LDH.

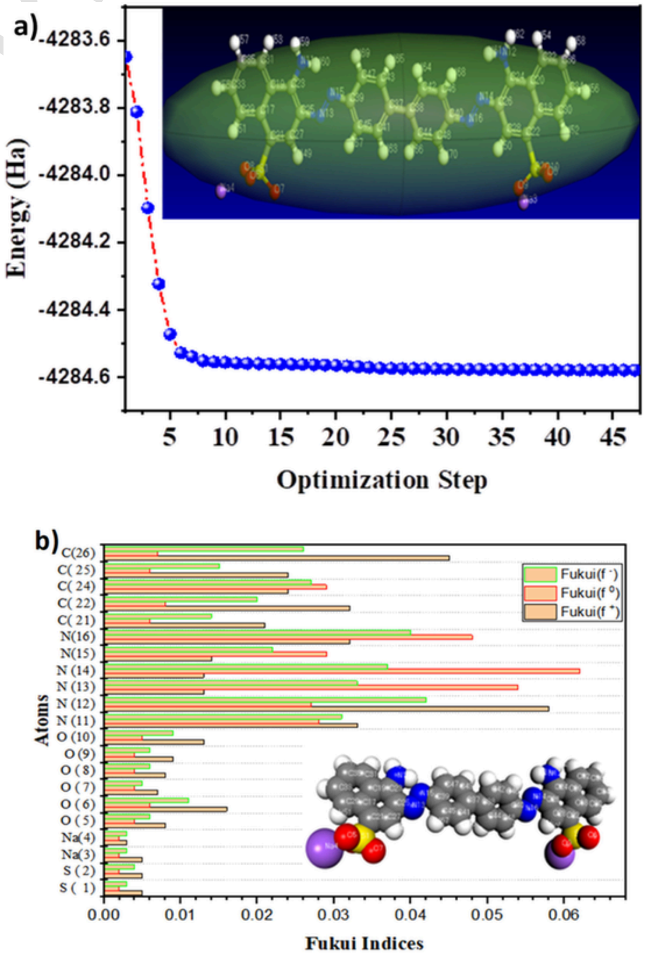

Fig. 11. a) Optimized molecular structure of the CR dye by DFT/SCAN. b) Fukui functions (f^{-},f^{+}, f^{0}), calculated via DFT/ SCAN module.

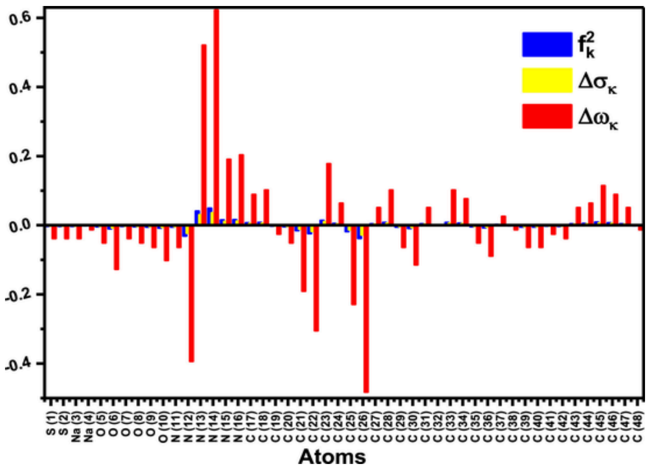

Fig. 12. The local dual descriptor, f_k^2, $\Delta\sigma_k$, and $\Delta\omega_k$of Congo Red, were determined using the DFT/SCAN method in aqueous solution.

faces in an aqueous medium. The total adsorption energies for Cu_2O/200H_2O, Cu_2O@Zn-Fe LDH/200H_2O, and Zn-Fe LDH/200H_2O, calculated using the locator model, are depicted in Fig. 14.

The electrostatic energy profiles in Fig. 14 exhibit distinct peaks and troughs, indicating varying electrostatic interactions between Congo Red (CR) molecules and semiconductor surfaces. Peaks correspond to regions of significant electrostatic attraction, facilitating CR adsorption through interactions like hydrogen bonding. Troughs represent areas of weaker interaction or repulsion, potentially hindering adsorption due to unfavorable orientations or surface features. Understanding these variations is crucial for identifying active sites that enhance photocatalytic degradation and for informing surface modifications to improve adsorption efficiency.

These simulations were conducted to investigate the dynamic behavior of CR, as illustrated in Fig. 15. It can be observed that the CR dye forms intermolecular hydrogen bonds through the sulfonate ion (SO_3^- Na^+), two azo groups (-*N* = *N*-), and two amino groups (-NH_2) during adsorption on the surface. As shown in Fig. 15**c**, the maximum interaction between the adsorbate (CR dye) and the adsorbent (the semiconductor surface), including the hydroxyl group on the LDH surface, results in higher adsorption energy of CR on the Zn–Fe LDH/200 H_2O surface, with a value of −37,789.80 kcal/mol. On Cu_2O@Zn-Fe LDH/200 H_2O, the CR dye bends on the surface of two LDH layers, and the adsorption energy was −23,768.99 kcal/mol, as shown in Fig. 15**b** However, on the Cu_2O/200 H_2O surface, the CR dye does not form bonds or only weak bonds are formed near the surface, resulting in an adsorption energy of −18,836.67 kcal/mol (Table 2). Moreover, H_2O molecules interfere with the CR dye, further hindering bond formation on the surface. Consequently, the adsorption energy is weak.

The MD simulations aimed to determine the bonding energies and interactions between CR molecules and semiconductors. The interaction energies (E_{int}) and bonding energies (E_{bind}) for CR on the semiconductor surfaces are presented in Table 3. The negative values of the interaction energies indicates that the system is more stable with stronger pollutant/semiconductor interaction. Conversely, the positive value of the bonding energy (E_{bind}) suggests more stable adsorption with greater affinity between the pollutant and the semiconductor.

In our study, the E_{bind} value reveals that CR dye adsorbs more spontaneously on the Zn-Fe LDH/200 H_2O surface compared to the two other semiconductors, Cu_2O@Zn-Fe LDH/200 H_2O and Cu_2O/200 H_2O. Additionally, the positive E_{bind} value is attributed to the hydrogen bonds on the surface, which are energetically more significant than van der Waals interactions. Therefore, these hydrogen bonds enhance the affinity and consequently the photodegradation of CR. Furthermore, we observed that the interaction energy (E_{int}) of CR on the Cu_2O/200H_2O surface is negative, indicating lower stability and a weak interaction between CR and the Cu_2O surface. Similar results were obtained using Monte Carlo simulations, confirming the energy order.

4. Conclusion

In this study, a Cu_2O@Zn-Fe LDH core-shell heterostructure was successfully synthesized using a coprecipitation method. The formation of Zn-Fe LDH and cuprite was confirmed through DRX, while SEM imaging revealed numerous Cu_2O nanocubes crystallizing in a cubic symmetry (Space Group Pn-3 m). An energy band diagram, derived from physical and electrochemical parameters, demonstrated the high photocatalytic efficiency of Cu_2O@Zn-Fe LDH across various pH levels. This efficiency was attributed to the Z-scheme mechanism under solar irradiation, facilitating the generation of reactive oxygen species that enabled complete degradation of Congo Red within 120 min. Furthermore, Density Functional Theory calculations using the SCAN functional provided insights into the optimized structure and predicted the reactivity sites of the Congo Red molecule. Fukui indices indicated that radical attacks predominantly occurred at active sites of the dye. Molecular Dynamics simulations further elucidated the adsorption behavior of Congo Red in an aqueous environment on Cu_2O@Zn-Fe LDH/200 H_2O, Zn-Fe LDH/200 H_2O, and Cu_2O/200 H_2O surfaces. The results showed a strong adsorption tendency of Congo Red on the Zn–Fe LDH/200 H_2O surface, with Monte Carlo simulations confirming the highest adsorption energy on this surface. Comparatively, the lower adsorption energy observed on the Cu_2O/200 H_2O surface underscores the crucial role of Zn–Fe LDH in the heterostructure, leading to enhanced dye degradation.

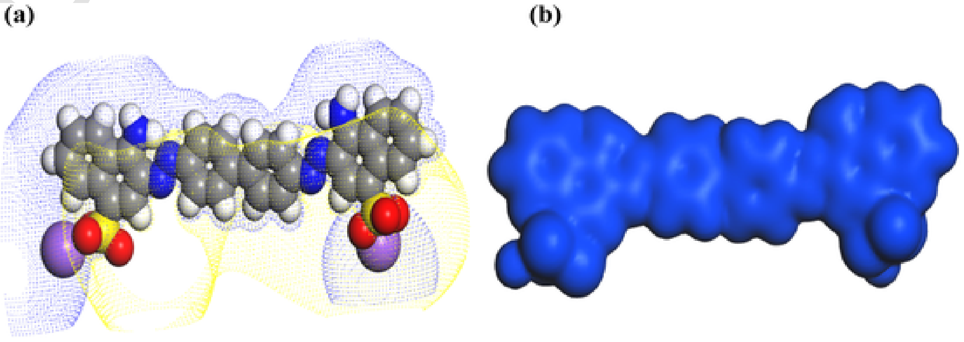

Fig. 13. a) electrostatic potential (MEP) (isovalue 0.016), **b)** electron density of Congo Red.

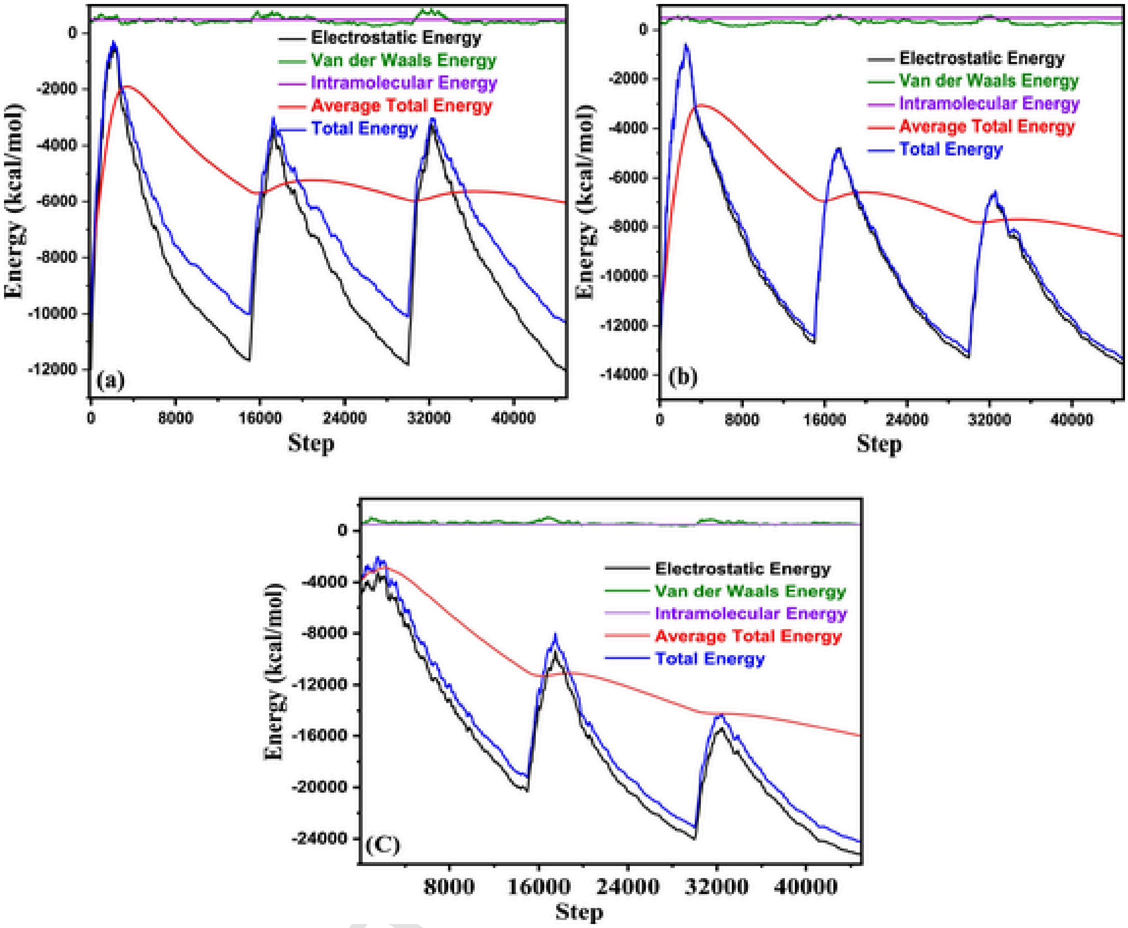

Fig. 14. The total energies adsorption for: **a)** $Cu_2O/200H_2O$, **b)** $Cu_2O@Zn\text{-}Fe$ LDH/$200H_2O$, and **c)** Zn-Fe LDH/$200H_2O$, using locator model calculations.

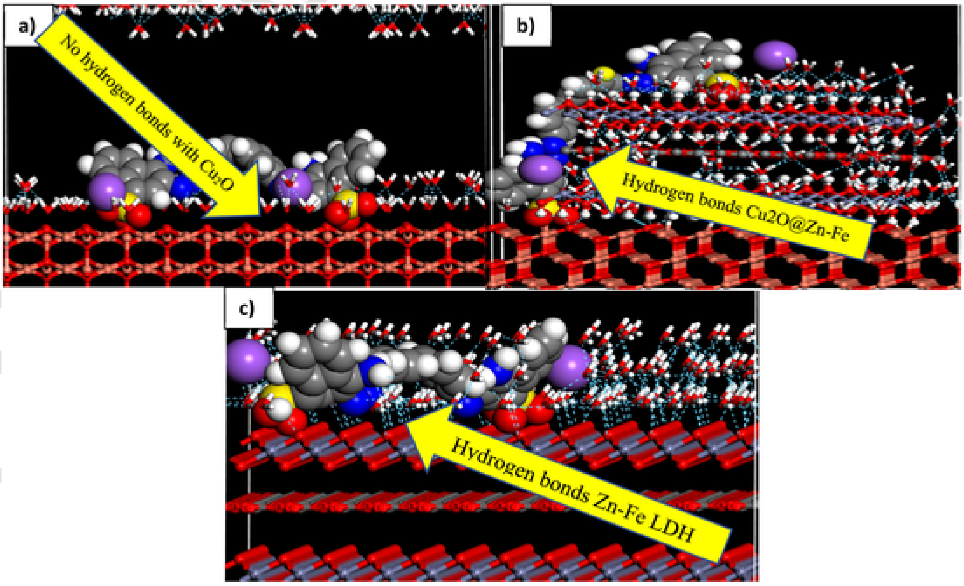

Fig. 15. The side and top views of the adsorption of Congo red (CR) dye on (a) $Cu_2O/200\ H_2O$, (b), $Cu_2O@Zn\text{-}Fe$ LDH/$200\ H_2O$ and (c) Zn-Fe LDH/$200\ H_2O$ surfaces, as found from the Dynamic simulation and Monte Carlo simulations.

Table 2
Outputs and descriptors calculated by the Monte Carlo simulation for the adsorption of Congo Red dye on Cu_2O /200 H_2O, Cu_2O @ Zn-Fe LDH/200 H_2O and Zn-Fe LDH /200 H_2O surfaces.

Compounds	Adsorption energy (kcal.mol^{-1})	Rigid adsorption energy (kcal.mol^{-1})	Deformation energy (kcal.mol^{-1})	dE_{ad} / dN_i (kcal.mol^{-1})
Cu_2O /200 H_2O	−18,836.67	−21,043.93	2207.256	−764.985
Cu_2O @ Zn-Fe LDH/200 H_2O	−23,768.99	−27,923.24	4154.253	−1500.209
Zn-Fe LDH /200H_2O	−37,789.80	−46,858.42	9068.624	−1746.02

Table 3
Output descriptors were calculated from molecular dynamics simulations for the adsorption of CR on semiconductor surfaces.

Compounds	binding energy (kcal.mol^{-1})	Interaction energy (kcal.mol^{-1})
Cu_2O /200 H_2O	−3763.84	3763.84
Cu_2O @ Zn-Fe LDH/200 H_2O	6104.16	−6104.16
Zn-Fe LDH /200H_2O	112,331.46	−112,331.46

CRediT authorship contribution statement

S. Kiamouche: Writing – original draft, Investigation, Formal analysis, Conceptualization. **L. Messaadia:** Writing – review & editing, Supervision, Software, Data curation, Conceptualization. **M. Benamira:** Writing – review & editing, Validation, Investigation, Formal analysis. **H. Lahmar:** Validation, Investigation, Formal analysis. **A. Hamdache:** Formal analysis, Data curation. **S.E. Drif:** Formal analysis, Data curation. **M. Trari:** Writing – review & editing, Validation, Supervision.

Declaration of competing interest

The authors declare that they have no known competing financial interests or personal relationships that could have appeared to influence the work reported in this paper.

Acknowledgment

The authors acknowledge the financial support from the Algerian Thematic Agency for Research in Science and Technology (ATRST) for the project PRFU No. B00L01UN180120220001 and B00L01UN180120230002.

Data availability

Data will be made available on request.

Supplementary materials

Supplementary material associated with this article can be found, in the online version, at doi:10.1016/j.molstruc.2025.142701.

References

[1] H. Boulahbel, M. Benamira, F. Bouremmad, N. Ahmia, S. Kiamouche, H. Lahmar, A. Souici, M. Trari, Enhanced photodegradation of Congo red dye under sunlight irradiation by p-n $NiFe_2O_4/TiO_2$ heterostructure, Inorg. Chem. Commun. 154 (2023) 110921, https://doi.org/10.1016/J.INOCHE.2023.110921.
[2] S. Merrad, M. Abbas, R. Brahimi, B. Bellal, M. Trari, Synthesis, characterization and application of tetragonal $BaTiO_{3-\delta}$ in adsorption and photocatalysis of Congo Red, Mater. Today Commun. 35 (2023) 105958, https://doi.org/10.1016/J.MTCOMM.2023.105958.
[3] S. El Bourachdi, F. Moussaoui, A. raza Ayub, A. El Amri, F. El Ouadrhiri, A. Adachi, A. Bendaoud, A.M. Idrissi, A. Lahkimi, DFT theoretical analysis, experimental approach, and RSM process to understand the congo red adsorption mechanism on Chitosan@graphene oxide beads, J. Mol. Struct. 1321 (2025) 140090, https://doi.org/10.1016/j.molstruc.2024.140090.
[4] S. Douafer, H. Lahmar, R. Laouici, F.Z. Akika, M. Trari, I. Avramova, M. Benamira, Synthesis and characterization of $CdFe_2O_4$ nanoparticles: application for the removal of Methyl Green under solar irradiation, Mater. Today Commun. 35 (2023) 105630, https://doi.org/10.1016/j.mtcomm.2023.105630.
[5] D. Chaibeddra, M. Benamira, M. Colmont, H. Boulehbal, H. Lahmar, I. Avramova, M. Trari, Synthesis, physical and electrochemical characterization of $CoCr_2O_4$ and its application as photocatalyst under solar irradiation, Inorg. Chem. Commun. 155 (2023) 111116, https://doi.org/10.1016/j.inoche.2023.111116.
[6] S. Kiamouche, L. Messaadia, H. Lahmar, G. Rekhila, M. Trari, M. Benamira, Enhanced photocatalytic degradation of Ponceau S red dye on the novel hetero-system Fe_2O_3/WO_3 under solar light irradiation, React. Kinet. Mech. Catal. 135 (2022) 3411–3426, https://doi.org/10.1007/s11144-022-02313-8.
[7] L. Messaadia, S. Kiamouche, H. Lahmar, R. Masmoudi, H. Boulahbel, M. Trari, M. Benamira, Solar photodegradation of rhodamine B dye by Cu_2O/TiO_2 heterostructure: experimental and computational studies of degradation and toxicity, J. Mol. Model. 29 (2023) 38, https://doi.org/10.1007/s00894-023-05449-z.
[8] H.-T. Vuong, T. Mahvelati-Shamsabadi, T.T. Dang, Q.D. Dao, E.W. Shin, J.S. Chung, Bandgap control of p-n heterojunction of Cu–Cu_2O @ ZnO with modified reduced graphene oxide nanocomposites for photocatalytic hydrogen evolution, Int. J. Hydrog. Energy 47 (2022) 23249–23263, https://doi.org/10.1016/j.ijhydene.2022.05.139.
[9] J. Wang, Y. Zhu, X. Zhong, Z. Hu, W.-H. Huang, C.-W. Pao, H. Cheng, N. Alonso-Vante, J. Ma, Universal synthesis strategy for preparation of transition metal oxide electrocatalysts doped with noble metal single atoms for oxygen evolution reaction, Energy Adv. 3 (2024) 2002–2012, https://doi.org/10.1039/D4YA00238E.
[10] R. Yu, Q. Chen, W. Li, X. Yu, Q. Zhong, Decorating Cu_2O with Ni-doped metal organic frameworks as efficient photocathodes for solar water splitting, Int. J. Hydrog. Energy 48 (2023) 17065–17073, https://doi.org/10.1016/j.ijhydene.2023.01.145.
[11] P. Guo, D. Yu, C. Zhao, J. Wang, J. Cheng, W. Fan, T. Ma, T. Gao, J. Li, Photo-fenton catalysis degradation of 4-dodecylmorpholine by heterogeneous microprocessor Cu_2O/SnO_2, J. Env. Chem. Eng. 12 (2024) 114682, https://doi.org/10.1016/j.jece.2024.114682.
[12] I. Stijepović, M. Milanović, M. Novaković, Cubic structured core/shell $NiFe_2O_4$@$ZnFe_2O_4$ nanocomposite: structural, morphological and magnetic properties, Ceram. Int. 50 (2024) 31326–31334, https://doi.org/10.1016/J.CERAMINT.2024.05.436.
[13] J. Song, W. Ge, S. Deng, J. Tang, S. Deng, P. Yang, Construction of Au nanoparticles decorated on $ZnFe_2O_4$@$ZnIn_2S_4$ core-shell structure to enhance photocatalytic hydrogen production, Colloids Surf. Physicochem. Eng. Asp. 705 (2025) 135705, https://doi.org/10.1016/j.colsurfa.2024.135705.
[14] S.Rai Shreya, P. Phogat, R. Jha, S. Singh, Synergistic effects of Carbon@MoS_2 core-shell nanostructures on charge dynamics for future optoelectronic applications, Mater. Chem. Phys. 329 (2025) 130147, https://doi.org/10.1016/j.matchemphys.2024.130147.
[15] X. Wang, G. Xu, Z. Zhou, X. Qin, Y. Su, X. Zhang, W. Wu, Cu_2O@TiO_2 core-shell microspheres for naphthalene oxidation, J. Porous Mater. 30 (2023) 1295–1302, https://doi.org/10.1007/s10934-023-01423-5.
[16] P. Karthikeyan, S. Meenakshi, Development of sodium alginate@ZnFe-LDHs functionalized beads: adsorption properties and mechanistic behaviour of phosphate and nitrate ions from the aqueous environment, Environ. Chem. Ecotoxicol. 3 (2021) 42–50, https://doi.org/10.1016/J.ENCECO.2020.11.003.
[17] S. Lu, Y. Yin, J. Bao, H. Wang, Z. Lei, E. Hu, Q. Xin, Y. Quan, J. Li, Q. Wang, CdS@NiCr-LDH Z-scheme heterojunction with high adsorption–photocatalysis for uranium(VI) removal without any sacrificial agent, J Env. Chem Eng 12 (2024) 112989, https://doi.org/10.1016/j.jece.2024.112989.
[18] D. Téllez-Flores, M. Sánchez-Cantú, F. Tzompantzi, A.G. Romero-Villegas, C. Tzompantzi-Flores, J.E. Carrera-Crespo, R. Pérez-Hernández, E. Rubio- Rosas, Influence of the Zn/Al molar ratio over the photocatalytic hydrogen production by ZnS/ZnAl-LDH composites, Int J Hydrog. Energy (2024), https://doi.org/10.1016/J.IJHYDENE.2024.01.069.
[19] H. Li, D. Liu, J. Chen, J. Zhu, P. Han, Effects of amino alcohols-intercalated MgAl-LDH nanocomposites on the properties of sulfoaluminate cement-based materials, Constr. Build. Mater. 452 (2024) 138982, https://doi.org/10.1016/J.CONBUILDMAT.2024.138982.
[20] A. Jebli, A. El Amri, R. Hsissou, A. Lebkiri, B. Zarrik, F.Z. Bouhassane, E. mahdi Hbaiz, E.H. Rifi, A. Lebkiri, Synthesis of a chitosan@hydroxyapatite composite hybrid using a new approach for high-performance removal of crystal violet dye in aqueous solution, equilibrium isotherms and process optimization, J. Taiwan. Inst. Chem. Eng. 149 (2023) 105006, https://doi.org/10.1016/J.JTICE.2023.105006.
[21] O. Doughmi, M. Salihi, A. Hsini, R. Hsissou, H. Moussout, A. Albourine, A. Shaim, Development and investigation of a new polyaniline@oak acorn biocomposite as a potential adsorbent for efficiently removing orange G dye from aqueous solution, Mater. Sci. Eng.: B 307 (2024) 117493, https://doi.org/10.1016/J.MSEB.2024.117493.
[22] J. Bensalah, A. Idrissi, M. El Faydy, G. Doumane, A. Staoui, R. Hsissou, A. Lebkiri, A. Habsaoui, Z. Abdelkader, E.H. Rifi, Investigation of the cationic resin as a potential adsorbent to remove MR and CV dyes: kinetic, equilibrium isotherms studies and DFT calculations, J. Mol. Struct. 1278 (2023) 134849, https://doi.org/10.1016/J.MOLSTRUC.2022.134849.
[23] A. Dabagh, R. Benhiti, M. EL-Habacha, A. Ait Ichou, M. Abali, A. Assouani, M.

Guellaa, A. Berisha, R. Hsissou, F. Sinan, M. Zerbet, Application of Taguchi method, response surface methodology, DFT calculation and molecular dynamics simulation into the removal of orange G and crystal violet by treated biomass, Heliyon. 9 (2023) e21977, https://doi.org/10.1016/J.HELIYON.2023.E21977.

[24] L. Kadiri, A. Ouass, R. Hsissou, Z. Safi, N. Wazzan, Y. Essaadaoui, I. Lebkiri, O. El Khattabi, E. Housseine Rifi, A. Lebkiri, Adsorption properties of coriander seeds: spectroscopic kinetic thermodynamic and computational approaches, J. Mol. Liq. 343 (2021) 116971, https://doi.org/10.1016/J.MOLLIQ.2021.116971.

[25] M. Shukla, S. Pal, I. Sinha, Ionic liquid functionalized Cu_2O nanoparticles, J. Mol. Struct. 1262 (2022) 132961, https://doi.org/10.1016/j.molstruc.2022.132961.

[26] M. Shi, Z. Zhou, Q. Li, Q. Liao, W. Yang, M. Si, Z. Yang, Q. Wang, ZnFe-LDH synthesized by seed-induced method to simultaneous enhance arsenic removal, stabilization and sludge reduction, J. Hazard. Mater. 480 (2024) 136459, https://doi.org/10.1016/J.JHAZMAT.2024.136459.

[27] X. gang Yang, Y. Li, F. Kong, X. Sun, S. Wang, Y. Cui, Effect of ZnFe-LDHs modified oyster shell on the removal of tetracyclines antibiotics and variation of tet genes in vertical flow constructed wetlands, Chem. Eng. J. 431 (2022) 134093, https://doi.org/10.1016/J.CEJ.2021.134093.

[28] Y. Xie, C. Chen, C. Zhang, L. Xu, Z. Li, W. Ren, X. Xu, Y. Ren, J. Lin, A. Wu, Synergistic enhancement of ultrahigh SERS activity via Cu_2O@Ag Core-Shell structure for accurate label-free identification of breast tumor subtypes, Nano Today 54 (2024) 102140, https://doi.org/10.1016/J.NANTOD.2023.102140.

[29] BIOVIA Support, Dassault Systemes Materials Studio Tutorials, BIOVIA Support, San Diego, CA 92121, USA, 2017.

[30] J. Padmanabhan, R. Parthasarathi, U. Sarkar, V. Subramanian, P.K. Chattaraj, Effect of solvation on the condensed Fukui function and the generalized philicity index, Chem. Phys. Lett. 383 (2004) 122–128, https://doi.org/10.1016/J.CPLETT.2003.11.013.

[31] J. Oláh, C. Van Alsenoy, A.B. Sannigrahi, Condensed Fukui functions derived from stockholder charges: assessment of their performance as local reactivity descriptors, J. Phys. Chem. A 106 (2002) 3885–3890, https://doi.org/10.1021/jp014039h.

[32] J.I. Martínez-Araya, Why is the dual descriptor a more accurate local reactivity descriptor than Fukui functions? J. Math. Chem. 53 (2015) 451–465, https://doi.org/10.1007/s10910-014-0437-7.

[33] R. Hsissou, F. Benhiba, M. El Aboubi, S. Abbout, Z. Benzekri, Z. Safi, M. Rafik, H. Bahaj, M. Kaba, M. Galai, N. Wazzan, S. Briche, S. Boukhris, A. Zarrouk, M. EbnTouhami, M. Rafik, Synthesis and performance of two ecofriendly epoxy resins as a highly efficient corrosion inhibition for carbon steel in 1 M HCl solution: DFT, RDF, FFV and MD approaches, Chem. Phys. Lett. 806 (2022) 139995, https://doi.org/10.1016/J.CPLETT.2022.139995.

[34] O. Allam, M. Maghsoodi, S.S. Jang, S.D. Snow, Unveiling competitive adsorption in TiO_2 photocatalysis through machine-learning-accelerated molecular dynamics, DFT, and experimental methods, ACS. Appl. Mater. Interfaces. 16 (2024) 36215–36223, https://doi.org/10.1021/acsami.4c02334.

[35] R.L.C. Akkermans, N.A. Spenley, S.H. Robertson, COMPASS III: automated fitting workflows and extension to ionic liquids, Mol. Simul. 47 (2021) 540–551, https://doi.org/10.1080/08927022.2020.1808215.

[36] R. Bendaas, Y. Bekkar, L. Messaadia, L. Bourougaa, A. Messaoudi, S. Kiamouche, B. Messaoud, Computational-based investigation of antioxidative potential polyphenolic compounds of Salvia officinalis L.: combined DFT and molecular docking approaches, J. Mol. Model. 30 (2024) 87, https://doi.org/10.1007/s00894-024-05866-8.

[37] Y. Wang, L. Wang, Z. Xiao, S. Liu, J. Hu, X. Long, L. Wu, C. Sun, K. Chen, F. Jiao, Construction of Z-scheme heterojunction of $(BiO)_2CO_3$/ZnFe-LDH for enhanced photocatalytic degradation of tetracycline, J. Alloys. Compd. 900 (2022) 163450, https://doi.org/10.1016/J.JALLCOM.2021.163450.

[38] H. Lahmar, M. Benamira, S. Douafer, F.Z. Akika, M. Hamdi, I. Avramova, M. Trari, Photocatalytic degradation of crystal violet dye on the novel $CuCr_2O_4/SnO_2$ hetero-system under sunlight, Opt. (Stuttg) 219 (2020) 165042, https://doi.org/10.1016/J.IJLEO.2020.165042.

[39] H. Lahmar, S. Douafer, R. Laouici, M. Hamdi, A. Souici, M. Trari, M. Benamira, Synthesis and characterization of $CuAl_2O_4$ nanoparticles: application for the removal of eriochrome Black T under solar light irradiation, Inorg. Chem. Commun. 163 (2024) 112316, https://doi.org/10.1016/J.INOCHE.2024.112316.

[40] A. Norouzi, A. Nezamzadeh-Ejhieh, Investigation of the simultaneous interactions of experimental variables and mechanism pathway in the photodegradation of methylene blue by binary ZnO/Cu_2O photocatalyst, Mater. Res. Bull. 164 (2023) 112237, https://doi.org/10.1016/J.MATERRESBULL.2023.112237.

[41] R. Keyikoglu, A. Khataee, H. Lin, Y. Orooji, Vanadium (V)-doped ZnFe layered double hydroxide for enhanced sonocatalytic degradation of pymetrozine, Chem. Eng. J. 434 (2022) 134730, https://doi.org/10.1016/J.CEJ.2022.134730.

[42] Q. Xu, L. Zhang, B. Cheng, J. Fan, J. Yu, S-scheme heterojunction photocatalyst, Chem. 6 (2020) 1543–1559, https://doi.org/10.1016/j.chempr.2020.06.010.

[43] M. Naderi, R. Darvishi Cheshmeh Soltani, Hybrid of ZnFe layered double hydroxide/nano-scale carbon for activation of peroxymonosulfate to decompose ibuprofen: thermodynamic and reaction pathways investigation, Env. Technol. Innov. 24 (2021) 101951, https://doi.org/10.1016/j.eti.2021.101951.

[44] S.R. Bhabal, N.G. Shimpi, Photocatalysis: mechanism, classification and basic principles, in: 2024: pp. 25–46. https://doi.org/10.1007/978-3-031-66260-7_2.

[45] N. Ahmia, M. Benamira, L. Messaadia, M. Colmont, H. Boulahbel, H. Lahmar, A. Souici, M. Trari, Photocatalytic activity of $ZnMn_2O_4/TiO_2$ heterostructure under solar light irradiation: experimental and theoretical study, J. Mol. Struct. 1306 (2024) 137834, https://doi.org/10.1016/J.MOLSTRUC.2024.137834.

[46] C. Li, H. Jing, Z. Wu, D. Jiang, Layered double hydroxides for photo(electro)catalytic applications: a mini review, Nanomaterials 12 (2022) 3525, https://doi.org/10.3390/nano12193525.

[47] A. Pastor, F. Rodriguez-Rivas, G. de Miguel, M. Cruz-Yusta, F. Martin, I. Pavlovic, L. Sánchez, Effects of Fe^{3+} substitution on Zn-Al layered double hydroxides for enhanced NO photochemical abatement, Chem. Eng. J. 387 (2020) 124110, https://doi.org/10.1016/J.CEJ.2020.124110.

[48] D. Abdessemed, S. Kiamouche, G. Nezzal, Comparison of the purifying performances of membrane bioreactor lab scale with activated sludge treatment, Open Environ. Eng. J. 2 (2009) 104–108, https://doi.org/10.2174/1874829500902010104.

[49] Y. Boughoues, M. Benamira, L. Messaadia, N. Bouider, S. Abdelaziz, Experimental and theoretical investigations of four amine derivatives as effective corrosion inhibitors for mild steel in HCl medium, RSC. Adv. 10 (2020) 24145–24158, https://doi.org/10.1039/D0RA03560B.

[50] S. Abdelaziz, M. Benamira, L. Messaadia, Y. Boughoues, H. Lahmar, A. Boudjerda, Green corrosion inhibition of mild steel in HCl medium using leaves extract of Arbutus unedo L. plant: an experimental and computational approach, Colloids Surf. Physicochem. Eng. Asp. 619 (2021) 126496, https://doi.org/10.1016/J.COLSURFA.2021.126496.